

FRPM/FMCAS Application for Prediction of Wind Turbine Noise

Alexandre Suryadi*, Florian Nils Schmidt, Christina Appel,
Nils Reiche, Roland Ewert, Michaela Herr, Jochen Wild

German Aerospace Center
Institute of Aerodynamics and Flow Technology
Lilienthalplatz 7, 38108 Braunschweig

*alexandre.suryadi@dlr.de

May 4, 2021

Abstract

The wind energy industry is moving towards larger rotor blades. Larger rotors will experience more substantial and more dynamic loads due to the fluctuating and heterogeneous wind field. The project *SmartBlades 2.0* investigates rotor blade design concepts that alleviate aerodynamic loading using active and passive mechanisms. As part of the project, acoustic evaluation is embedded in the design process. The present work evaluates two concepts for load alleviation separately, an inboard slat and an outboard flap, using FRPM/FMCAS (Fast Random Particle Mesh/Fast Multipole Code for Acoustic Shielding) numerical prediction toolchain developed at DLR.

The numerical tools are validated using the experimental results of an active trailing-edge of small-scale model measured in the Acoustic Wind tunnel Braunschweig (AWB). The active trailing-edge, designed as a plain flap, generates flap side-edge noise. The FRPM/FMCAS tool was able to produce a comparable sound spectrum for the negative flap deflection. Whereas, for the positive flap deflection, the experimental result is obfuscated by the adverse pressure gradient effect.

The self-noise from a slat at the inboard section of a rotor blade with a 44.45 m radius was investigated and compared with that from the outboard trailing-edge using FRPM/FMCAS. Furthermore, the rotational effect of the rotor was included in the post-processing to emulate the noise observed at ground level. The findings show an increase in the slat's overall sound pressure level and a maximum radiation upwind of the wind turbine for the case with the largest wind speed that represents the off-design condition. In operational conditions, the slat adds at most 2 dB to the overall sound pressure level.

The toolchain evaluates wind turbine noise with conventional or unconventional blade design, and the problem can be scaled up for a full-scale analysis. As such, the tools presented can be used to design low-noise wind turbines efficiently.

1 Introduction

Wind turbine development is trending towards larger rotor diameters. With a large rotor, the turbine generates more power. However, it will also experience an increased aerodynamic load. One of the well-established systems for wind turbine control is the blade pitch control. Controlling the blade's pitch angle avoids excessive loads on the blades and increases the lifespan of the wind turbine [1]. However, with large rotors, the range of the problem's scale from the blade's hub to its tip becomes larger and local controls are appealing. Concepts for local load control are investigated in the project *SmartBlades 2.0*, the acoustic performance

of two of which are explored numerically in this paper: (i) an active trailing-edge at the outboard rotor and (ii) a rigid slat at the inboard rotor.

For validation of the numerical procedure, flap side-edge noise was simulated using FRPM/FMCAS (Fast Random Particle Mesh/Fast Multipole Code for Acoustic Shielding). The flap side-edge noise is generated due to the plain flap's deflection as part of the active trailing-edge concept. For this case, experimental results are available for comparison. Measurements were conducted in the acoustic wind tunnel Braunschweig (AWB), located at the German Aerospace Center's (DLR) Braunschweig site. For a description of the measurements and a discussion of the results, the reader is referred to Ref. [2].

The slat is positioned upstream of the leading edge of the inboard rotor. The flow leaving the slat is accelerated and delays the stall of the inboard rotor segment. The goal of this study is to rank the slat's self-noise relative to the trailing-edge noise of the outboard blade segment of the same rotor, with the analysis focusing on 1 m span blade segments.

In this paper, a brief description of the numerical methods is provided in the next section. Next, the numerical tools are validated using flap side-edge noise, where measured results are available. This section is followed by the setup and calculation of the inboard slat noise and outboard trailing-edge noise. In the next section, the sound immission is calculated for an arbitrarily positioned ground observer. Finally, a conclusion of the work is drawn.

2 Numerical procedure

2.1 Fast Random Particle Mesh Method

Synthetic turbulence is generated using the Fast Random Particle Mesh (FRPM) method under the assumption of isotropic turbulence. The local mean flow information from Reynolds-Averaged Navier-Stokes (RANS) are used to assign a turbulent eddy's scale and strength. Only a small volume of RANS around a noise radiating edge was used to reconstruct the turbulence field. Finally, the enstrophy potential generated by FRPM is compared against its ideal (isotropic) counterpart. A summary of the FRPM simulation setup particular to this task is given below. For a complete description, the authors suggest the following Refs. [3, 4, 5, 6].

Equation (1) is a system of equations governing the acoustic perturbation expressed as the fluctuating density ρ' . The sound pressure is defined as $p' = a_0^2 \rho'$, where $a_0^2 = \gamma p^0 / \rho^0$ is the square of the speed of sound with $\gamma = 1.4$ the adiabatic. The remaining variables p^0 and ρ^0 are the mean pressure and mean density, respectively. The sound pressure is expressed as a function of the mean flow u_i^0 , the fluctuating component u_i' , and the mean and fluctuating vorticity ω_i^0 and ω_i' ,

respectively. The subscripts i , j and k denote the index of a vector element.

$$\begin{aligned} \frac{\partial \rho'}{\partial t} + \frac{\partial}{\partial x_i} (\rho^0 u'_i + \rho' + u_i^0) &= 0, \\ \frac{\partial u'_i}{\partial t} + \frac{\partial}{\partial x_i} (u_j^0 u'_j) + \frac{\partial a_0^2 \rho'}{\partial x_i} &= -\varepsilon_{ijk} \omega_j^0 u'_k - \varepsilon_{ijk} \omega'_j u_k^0 - \varepsilon_{ijk} \omega'_j u'_k. \end{aligned} \quad (1)$$

Only the second term of the left hand side of Eqn. (1) is used as the sound source, *source B*, i.e. $q_B = \varepsilon_{ijk} \omega'_j u_k^0$, with ε_{ijk} the Levi-Civita symbol. The other two terms are neglected because q_B can well reproduce slat noise spectra [4]. Contrary to Ref. [4], in this work, q_B is also applied to trailing-edge noise due to the recent developments in defining the enstrophy variance [5].

The enstrophy is defined as

$$\zeta = \frac{1}{2} (\omega'_i \omega'_i) = \frac{\varepsilon}{\nu} - \frac{\delta^2 k_t}{\delta x_i \delta x_j} + \varepsilon_{ijk} \frac{d}{dx_i} \langle u'_j \omega'_k \rangle, \quad (2)$$

where ε is the turbulence decay rate, ν is the kinematic viscosity, k_t the turbulent kinetic energy. The last term on the right-hand side, a product of two fluctuating variables, is assumed to be small enough to be negligible. The enstrophy spectrum is related to the turbulent kinetic energy spectrum by the square of the wavenumber k^2 , because of the second derivative of the second term on the right-hand side Eqn. (2). The turbulent kinetic energy is modeled using Pope's model spectrum. Hence the enstrophy spectrum is

$$E_{M,\zeta} = \zeta c_{M,\zeta} \frac{k^4 \Lambda^2}{(1 + k^2 \Lambda^2)^2} \quad (3)$$

with Λ as the integral length scale. The normalization factor $c_{M,\zeta}$ expressed as

$$\begin{aligned} c_{M,\zeta} &= \left[\int_{k_{\min}}^{k_{\max}} \frac{k^4 \Lambda^2}{(1 + k^2 \Lambda^2)^2} dk \right]^{-1} \\ &= \frac{\Lambda^3}{2} \left[\frac{k_{\max} \lambda}{(1 + (k_{\max})^2) - 3 \arctan(k_{\max} \Lambda) + 2 k_{\max} \Lambda} \right]^{-1} \end{aligned} \quad (4)$$

with $k_{\min} = 0$ and $k_{\max} = (\varepsilon/\nu^3)^{1/4}$.

In application, the spectrum in Eqn. (3) is expressed as a superposition of weighted Gaussian functions

$$E_{M,\zeta}(k) = \bar{E} \int_0^\infty f(l, \Lambda) E_G(k, l) dl, \quad (5)$$

where $\bar{E}_{M,\zeta} = \int_0^\infty E_{M,\zeta}(k) dk$ and $\bar{E}_G = \int_0^\infty E_G(k,l) dk = 1$ with l the turbulence length scale and

$$f(l, \Lambda) = c_{M,\zeta} \frac{3}{4} \frac{\pi}{4l^2\Lambda^2} \exp\left(-\frac{l^2}{\pi\Lambda^2}\right) \quad (6)$$

$$E_G(k,l) = \frac{8k^4l^5}{3\pi^3} \exp\left(-\frac{k^2l^2}{\pi}\right). \quad (7)$$

The fluctuating components of turbulence are generated using the expression of the divergence-free fluctuating turbulence $\boldsymbol{\psi}'$

$$\boldsymbol{\psi}' = \nabla_x \times \left[A(\mathbf{x}) \int_{V_s^n} \mathbf{G}(\mathbf{x} - \mathbf{x}'') \mathbf{U}(\mathbf{x}'', t) d^n \mathbf{x}'' \right], \quad (8)$$

which is the convolution of a white noise field $\mathbf{U}(\mathbf{x}'', t) = \mathbb{U}_i(x''_i, t)$ with a spatial Gaussian filter kernel $\mathbf{G}(\mathbf{x} - \mathbf{x}'')$ inside an n -dimensional source region V_s^n . The white noise field satisfies

$$\langle \mathbb{U}(x'', t) \rangle = 0, \quad (9)$$

$$\langle \mathbb{U}_i(x'', t) \mathbb{U}_j(x'' + r, t) \rangle = \frac{1}{\rho_0} \delta_{ij} \delta(r - u_i^0 \tau) \quad (10)$$

in the Eulerian frame. The brackets $\langle \dots \rangle$ denote the ensemble average, δ_{ij} is the Kronecker delta and δ is the Dirac-delta function.

The Gaussian filter kernel $\mathbf{G}(\mathbf{x} - \mathbf{x}'')$ is a function of the turbulence length scale l

$$\mathbf{G}(\mathbf{x} - \mathbf{x}'') = \frac{1}{l^{n/2}} \exp\left(-\frac{\pi |\mathbf{x} - \mathbf{x}''|^2}{l^2}\right), \text{ where } l = l(x) = \frac{c_l}{C_\mu} \frac{\sqrt{k_t(x)}}{\omega(x)} \quad (11)$$

with k_t as the turbulent kinetic energy and ω as the specific dissipation rate, not to be confused with the vorticity ω'_i provided by the RANS simulation. The constants for the length scale are $c_l = 0.54$ and $C_\mu = 0.09$.

The function $A(\mathbf{x})$ scales the magnitude of the fluctuating quantity as

$$A(\mathbf{x}) = \sqrt{\frac{\rho_0 2^{4-n} l^2}{3\pi} \bar{E}(x)}, \quad (12)$$

where $\bar{E}(\mathbf{x})$ is the appropriate turbulence quantity. Namely, if $\boldsymbol{\psi}'$ refers to fluctuating velocity $\boldsymbol{\psi}' = k_t(\mathbf{x})$ is the turbulent kinetic energy. Alternatively, if $\boldsymbol{\psi}'$ refers to the fluctuating vorticity then $\bar{E}(\mathbf{x}) = \zeta(\mathbf{x})$ is the turbulent enstrophy. Using

the superposition of the weighted Gaussian function Eqn. (12), in discrete form, becomes

$$A_m(x) = \sqrt{\frac{\rho_0 2^{4-n} l_m^2}{3\pi}} \bar{E} f(l_m, \Lambda) \Delta l_m, \quad (13)$$

where \bar{E} has been substituted with $\int_0^\infty E_{M,\zeta}(k) dk$ and m denotes the i^{th} discrete length.

The FRPM patch is discretized using the following expression

$$\Delta x = \frac{a_0 Ma}{f_{\max} PPS_{FRPM}}, \quad (14)$$

where Δx is the FRPM characteristic length of the FRPM patch, Ma is the flow Mach number, f_{\max} is the maximum frequency to be resolved, and PPS_{FRPM} is the number of discrete points per wavelength usually taken as 6 points per wavelength.

The parameters required for the FRPM patch are: mean velocity field, turbulent kinetic energy k_t , mixing length scale $\ell = \sqrt{k_t/\omega}$ with ω the specific turbulence dissipation rate, the turbulence decay rate $\varepsilon = C_\mu k_t/\omega$ and turbulence enstrophy $\zeta = 6\varepsilon/\nu$.

2.2 Fast Multipole Code for Acoustic Shielding

The Fast Multipole Code for Acoustic Shielding [7, 8] is a numerical algorithm developed at the Department of Technical Acoustics in DLR-Braunschweig to calculate the sound radiation from a sound source close to a body using the boundary element method.

The Helmholtz equation relates the second order spatial derivative of the pressure \hat{p} to the sound source \hat{f} ,

$$(\nabla^2 + k)\hat{p}_x = -\hat{f}; x \in \Omega, \quad (15)$$

which can be solved using the free-field Green's function G_0 integrated over the domain Ω ,

$$\hat{p}_x - \int_{\partial\Omega} \left[\hat{p}_y - \frac{\partial G_0}{\partial n_y} - G_0 \frac{\partial \hat{p}_y}{\partial n_y} \right] d\Omega_y = \hat{p}_v, \quad (16)$$

the subscripts x and y indicate an observer's locations and a point on the surface, respectively. The right-hand side represents a volumetric contribution that does not appear in the problem statement, and thus it is neglected.

By applying a Neumann boundary condition to Eqn. (16) on the airfoil's surface, the pressure gradient normal to the surface is

$$\frac{\partial \hat{p}_y}{\partial n_y} = Y_y \hat{p}_y + V_y(\hat{u}_n), \quad (17)$$

where Y_y is the wall admittance and V_y is the surface excitation that is a function of the wall-normal component of the induced velocity \hat{u}_n . The Burton-Miller linear operator B_x was used to enforce a unique solution of the outer problem of surface $\partial\Omega$ leading to

$$\frac{1}{2}B_x\hat{p}_x - \int_{\partial\Omega} \left[\hat{p}_y \frac{\partial}{\partial n_y} - Y_y \right] B_x G_0 d\Omega_y = \int_{\partial\Omega} V_y(\hat{u}_n) B_x G_0 d\Omega_y. \quad (18)$$

Turbulence interaction with the surface is established by coupling acoustic and incompressible velocity $\hat{u}_{n,a} = \hat{u}_{n,i}$. The incompressible velocity $\hat{u}_{n,i}$ is induced by turbulence vorticity $\omega' = \omega'_i$ and can be obtained by solving the Poisson equation for the potential ψ' ,

$$\hat{u}_{n,i} = \mathfrak{F} \left(\mathbf{n} \cdot (\nabla \times \psi') \right); \nabla^2 \psi' = -\omega'. \quad (19)$$

Here, \mathbf{n} is the wall-normal vector and \mathfrak{F} indicates the Fourier transform. The turbulence vorticity ω' is synthesized using FRPM.

The discretization of the surface is expressed as

$$\Delta x = \frac{a_0}{f_{\max} PPW_{FMBEM}}, \quad (20)$$

where Δx is the cell's characteristic length, f_{\max} is the maximum frequency to be resolved, and PPW_{FMBEM} is the number of discrete points per wavelength usually taken as 6 points per wavelength.

The FMCAS simulation resolves the Helmholtz equation at each discrete and narrowband frequency. To further fasten the numerical process, the one-third octave band sound pressure level can be expressed in terms of the narrowband sound pressure level, where the center frequency of the third-octave band f_c can be expressed as a product of the narrowband frequency width ∂f and an integer multiplier i ,

$$L_{p,1/3}(f_c) = 10 \log_{10} \left(\frac{dp_{rms}^2(f_c)}{(20\mu\text{Pa})^2} \right), \quad (21)$$

with

$$dp_{rms}^2(f_c) = \Phi_{pp}(f_c) f_c \frac{\ln 2}{3} = \Phi_{pp}(f_c) \partial f i \frac{\ln 2}{3}. \quad (22)$$

Essentially, dp_{rms}^2 in Eqn. (22) is a narrow-band spectrum factored by $(\ln 2)/3$ so that the level is of the third-octave band spectrum. The relations above is derived in Appendix A

3 Active Trailing Edge

3.1 Numerical Setup

Measurements of the active trailing-edge were conducted in AWB using a blade section model with a chord length of 0.3 m and a span length 1.2 m. The wind tunnel model is equipped with a plain flap that has a chord length of 0.09 m and a span length of 0.4 m at the mid-span section. The numerical blade model is a half-span of the one used in the measurement. The symmetrical boundary condition was applied on the mid-span of the blade model. The flow field around the flap side-edge is shown in figure 1. Because of the sudden change of contour introduced by the deflected flap's side surface, a negative strength vortex develops for the negative flap deflection $\delta_f = -5^\circ$ and a positive strength one develops for $\delta_f = 5^\circ$. The RANS numerical setup is detailed in Ref. [2].

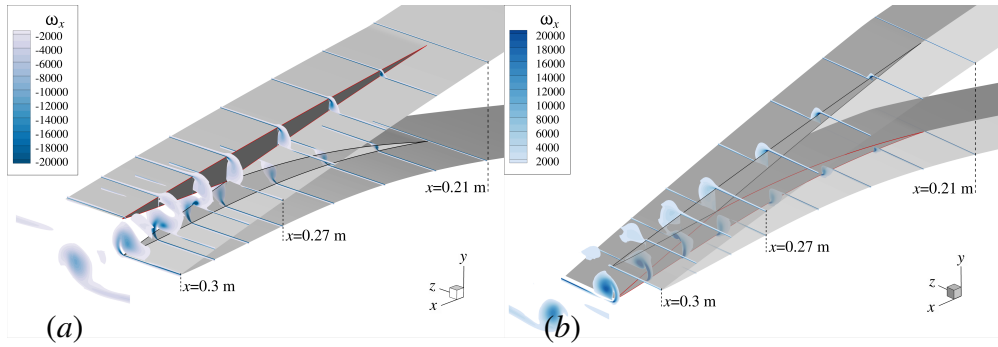


Figure 1: Vortical field around the flap side-edge (a) $\delta_f = -5^\circ$ and (b) $\delta_f = 5^\circ$.

The turbulence reconstruction from RANS is localized to a small volume around the radiating edge. First, a region encompassing the full span of the trailing-edge simulated in RANS and the flap side-edge was defined. The size of the first volume is $0.192 \text{ m} \times 0.064 \text{ m} \times 0.512 \text{ m}$. A cross-section of the RANS flow field around the trailing-edge is shown in figure 2(a). For a closer investigation of flap side-edge noise a local region encompassing the flap side-edge is defined and shown in figure 2(b). The size of the local volume is $0.192 \text{ m} \times 0.064 \text{ m} \times 0.064 \text{ m}$. Both volumes have a cell size of 0.002 m, such that the maximum frequency that FRPM can resolve is $f_{\max} \approx 8 \text{ kHz}$.

A spatial smoothing function with a Gaussian kernel is introduced to the FRPM input parameters to ensure smoothly distributed derivatives. Special care was taken to maintain zero values inside the solid. Another kernel is introduced in the FRPM patch to ensure that vorticities gradually gain or lose their energy when entering or leaving the patch, which is accomplished by introducing a \cos^2 ramp function at the sides of the volumetric patch.

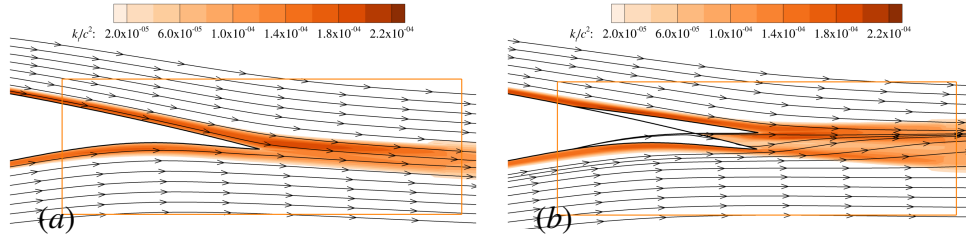


Figure 2: Cross-section of the FRPM patch (orange) of (a) trailing-edge (b) flap side-edge. The turbulent kinetic energy field and the two-dimensional streamlines are shown.

3.2 FRPM Turbulence Reconstruction

The reconstructed enstrophy from FRPM is shown in figure 3 for a cross-section of the trailing edge and the flap side-edge region. Overall, the reconstructed enstrophy approximates the target, isotropic turbulence enstrophy sufficiently well. The target enstrophy field and other turbulent parameters from RANS result from the integration of the turbulence spectrum from $k \rightarrow 0$ to the Kolmogorov scale wavenumber. The FRPM reconstructed field has a limited integration range, with the lower limit depends on the domain size and the upper limit on the cell size. The loss of spatial resolution is accounted for by tailoring the spectral content to the range of resolvable wavenumbers introduced in [9] and applied in [10, 11]. Here, the generalized turbulence spectrum is comprised of 7 superpositioned Gaussian spectra, and the turbulence spectrum model *Model-3*, following from Ref. [11], was chosen.

3.3 FMCAS Result

The measurement of the active trailing-edge was detailed in Ref. [2]. As a summary, the measured blade section's size, a DU08-W-180 profile, is 0.3 m in chord length and 0.09 m in plain flap chord length. The plain flap span length is one-third of the blade section's span length. Due to its small size, the noise sources' significance is judged by the noise reduction effects of materials that inhibit noise radiation. Namely, porous material was used on the flap side-edges, whereas the trailing-edge brush was used at the trailing edge. A porous material as a mean for noise reduction has been investigated thoroughly, for example Refs. [12, 13, 14]. The noise reduction potential for trailing-edge brush was investigated in Refs. [15, 16]. The sound pressure levels with the noise reduction material are compared with the reference edges to understand each noise source's significance. A key point in the measurement is that the flap side-edge noise is not a significant source of noise when the flap deflection angle is between -5° and 5° . It becomes a sig-

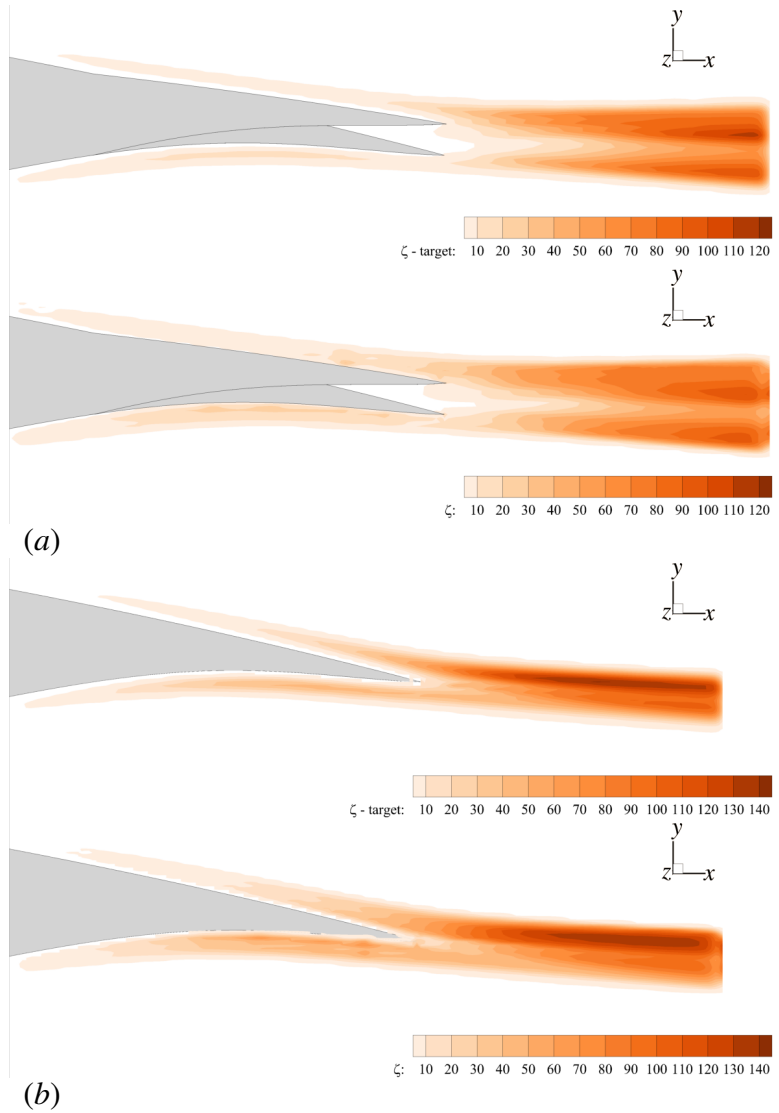


Figure 3: Reconstruction of the enstrophy for the FRPM patch given in figure 2 (a) flap side-edge and (b) trailing-edge.

nificant source of noise for the deflection angle of -10° and 10° . The noise was measured using an array consisting of 96 microphones, and the spectra were calculated by integrating the distributed power level produced by the deconvolution algorithm *CLEAN-SC*[17].

Figure 4 is a comparison between the sound pressure level spectra between the experiment and the simulation. Within a margin of error, because of the simulation's stochastic method, the numerical prediction produced a sound spectrum comparable to that of the experiments.

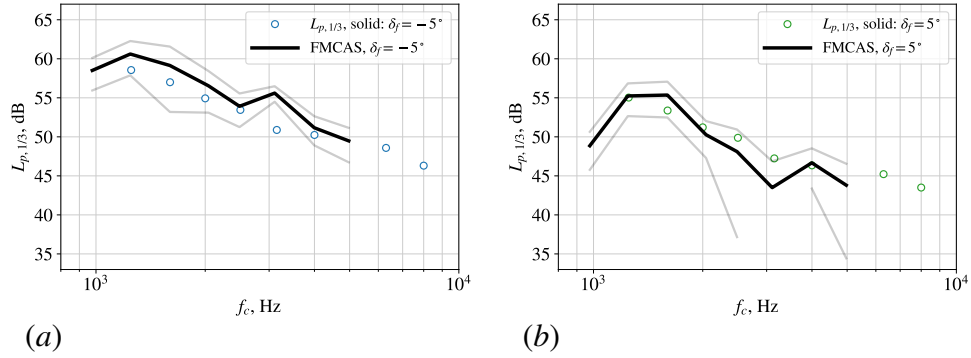


Figure 4: A comparison of the far-field sound pressure level between experiments and simulation encompassing the whole trailing-edge for (a) flap up and (b) flap down configuration.

As described in Eqn. (8), the fluctuating turbulence field is generated using a convolution integral of a white noise field and a spatial Gaussian filter kernel. A reliable average in this study was obtained by repeating the simulation 15 times and realizing a different white noise field each time. Each realization of the FRPM/FMCAS simulation of the trailing-edge region is shown as the blue line and round marker in figure 5. The ensemble averages of every 5, 10, and 15 realizations and the upper and lower confidence bounds (with 95% confidence) are shown in figure 5. The upper and lower confidence levels are approximately +1.5 dB and -3 dB, respectively. At least ten realizations are required to make a smooth averaged spectrum.

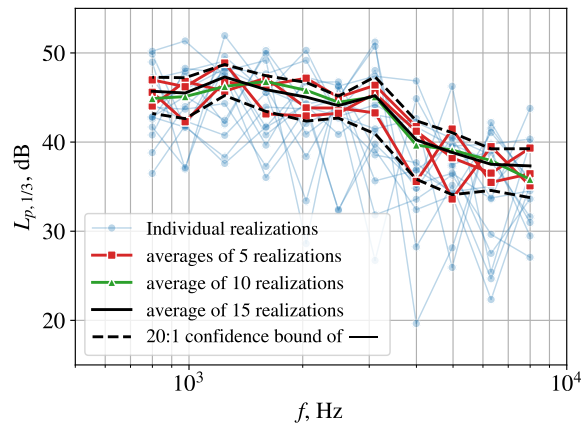


Figure 5: Stochasticity of the sound pressure level as a result of the random particle method.

The comparison of experimental and numerical sound pressure level spectra in figure 6 is localized to the flap side-edge. Figure 6 shows distinctively the frequency range of the flap side-edge noise $f_c > 3$ kHz for $|\delta_f| = 5^\circ$ and $f_c > 2$ kHz for $|\delta_f| = 10^\circ$, which is consistent with the previous study, where the flap side-edge noise scales with the characteristic radius of the flap side-edge vortex [18]. The measurement result of $\delta_f = -5^\circ$ is closer to the FRPM/FMCAS result, whereas at $\delta_f = 5^\circ$ FRPM/FMCAS result diverges from that of the measurement. A possible explanation of this discrepancy is that the flap's positive deflection adds to the thickness of the boundary layer and increases the level of the adverse pressure gradient. This explanation is consistent with the measurement of surface pressure of adverse pressure gradient boundary layer in Ref. [19], where the adverse pressure gradient increases the power spectral level in the low-frequency region.

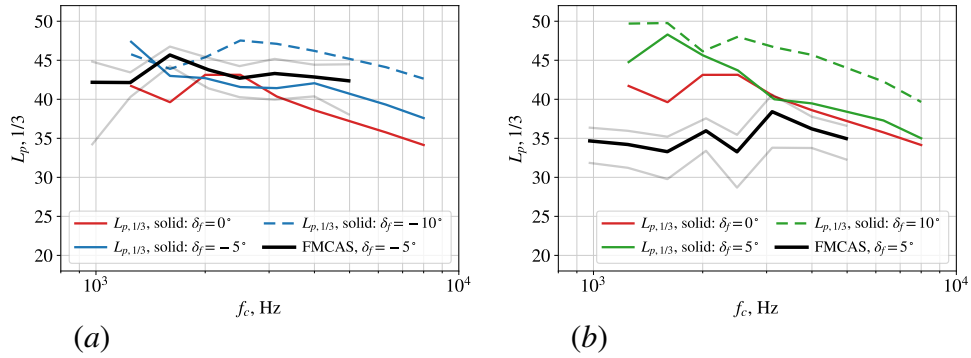


Figure 6: A comparison of the far-field sound pressure level between experiments and simulation focused around the flap side-edge region for (a) flap up $\delta_f = -5^\circ$ and (b) flap down configuration $\delta_f = 5^\circ$.

4 Rigid Inboard Slat

4.1 Numerical Setup

The investigated geometry is a wind turbine blade in combination with the rigid slat as shown in figure 7. The blade length is $\mathbb{R} = 44.45$ m, where one of them is shown in green and with the slat in blue. The rigid slat was designed in the forerunner project *SmartBlades* and is based on the investigations made by Manso Jaume and Wild[20]. The side of the blade facing the reader is the pressure side. The main blade element's trailing-edge is highlighted in red, and its leading-edge is in purple. The rotor's rotational velocity is $\Omega = \Omega \hat{e}_x$ and the wind speed is $\mathbf{U} = U_0 \hat{e}_x$.

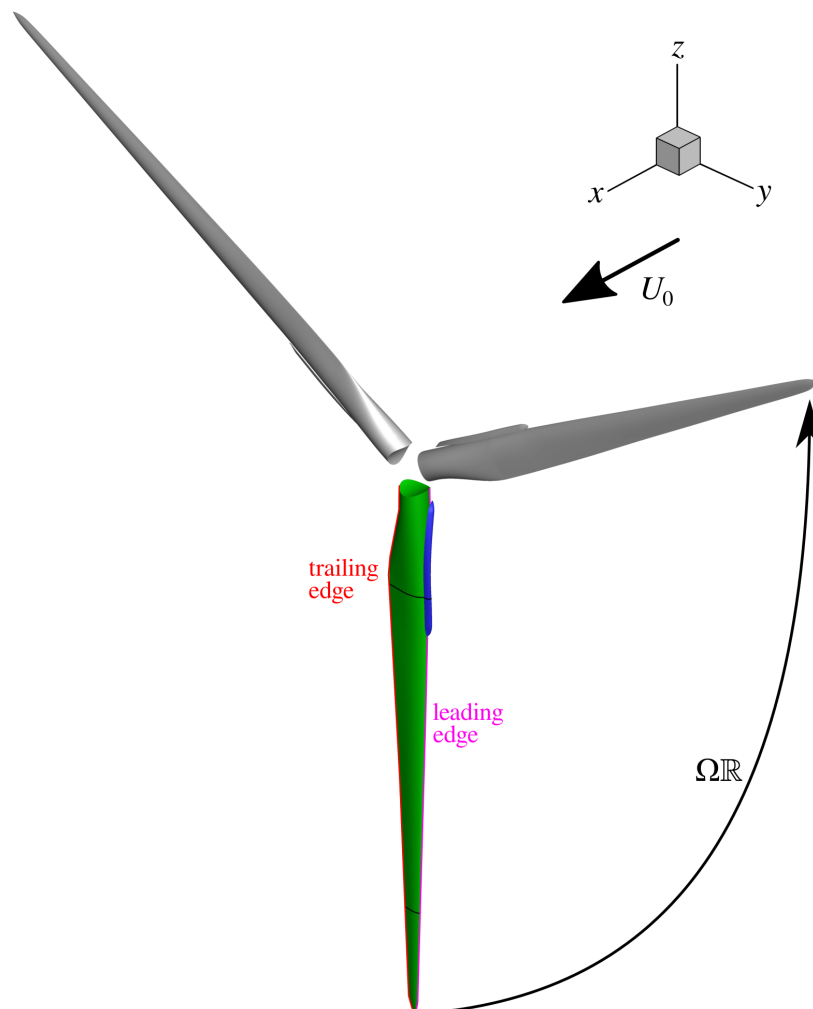


Figure 7: A sketch of the Suzlon S88 wind turbine excluding its tower and nacelle.

In the numerical flow simulations, the three rotor blades including the designed rigid slats were considered as an isolated geometry. Accordingly, the nacelle and the turbine tower were neglected in the studies. The surface of each rotor blade as well as the surface of each slat were meshed with ordered triangles, which were extruded as prism layers. The resolution of the boundary layer is obtained by 32 cells in the region normal to the wall. Hereby, the rotor blade as well as the slat were meshed with an O-topology with a first wall spacing that reaches the condition $y^+ \approx 1$. The prism layers are followed by tetrahedra, with which the entire far field is meshed. The far field is designed cylindrical with a length of $20\mathbb{R}$ and a radius of $10\mathbb{R}$. The whole computational grid of the three blades including its rigid slats consist of approximately 107 million points.

As mentioned before, the numerical investigations were made with the use of steady-state RANS simulations. The flow solver is the DLR TAU code [21], which is an unstructured finite-volume vertex-based CFD solver. The RANS simulations were run with the $k - \omega$ -SST turbulence model. The boundary layer of the rotor blades as well as the slats was assumed to be fully turbulent. The inflow was defined as uniform with a turbulence intensity of $Tu_{0,\infty} = 0.001$ at the far field boundary. The simulations were run for different wind speeds, whereby a fixed rotation speed and a fixed rotor pitch angle were set with reference to a control strategy designed by Suzlon. The parameters used in the numerical studies are listed in Table 1.

The 1 m span localized blade sections to be acoustically simulated are represented by the radial positions, R , of their mid-spans. The mid-span profiles are shown in figure 8. At $R = 10$ m, the slat's chord length is $c_s = 0.52$ m, and at $R = 36$ m, the outboard profile's chord length is $c_r = 1.428$ m. The blade and boundary layer parameters at R is tabulated in Table 1. In the design, the slat is attached to the blade by two support structures at $R = 4.25$ m and $R = 9.75$ m. These supports are not modeled in the simulation. Hence the resulting flow field is not affected by them. The acoustic analysis is centered on the slat's trailing-edge at $9.5 \text{ m} \leq R \leq 10.5 \text{ m}$ and the blade's trailing-edge at $35.5 \text{ m} \leq R \leq 36.5 \text{ m}$. Four wind speeds are defined for the simulation $U_0 = 4$ m/s, 6 m/s, 9 m/s and 16 m/s. The blade is also designed with a local twist angle θ_{tw} , such that the angle that the chord line makes with the x -axis is $\theta = \theta_p + \theta_{tw}$. Additionally, relative to the blade's chord line, the slat's chord line has an initial angle of 8.46° . The local inflow velocity is defined as $\mathbf{U}_{0,1} = U_0(1 - a)\hat{e}_x + \Omega R(1 + a')\hat{e}_y$, where $a = 0.33$ is the axial induction factor and $a' = (1 - 3a)/(4a - 1)$ is the tangential induction factor.

FRPM assumes a stationary model in a steady flow, hence the RANS field has to be transformed to conform. The velocity relative to the moving blade $u^0 = u^{0*}$, $v^0 = v^{0*} - \Omega R \cos(\arctan(y/z))$ and $w^0 = w^{0*} + \Omega R \sin(\arctan(y/z))$ with u^{0*} , v^{0*} and w^{0*} are the mean velocity vector components relative to a stationary observer

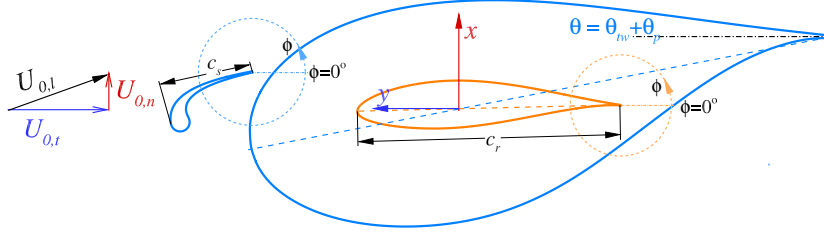


Figure 8: The slat, the inboard, $R = 10$ m, and the outboard, $R = 36$ m, sections of the blade.

in x , y , and z -directions, respectively. The flow streamlines and pressure coefficients of the two blade sections in Table 1 are shown in figures 9, 10 and 11, respectively. The pressure coefficient is $c_p = p_s^0 / (0.5\rho U_{0,l}^2)$, where p_s^0 is the static pressure on the surface. The color contour in these figures represents the turbulence kinetic energy normalized with the square of the speed of sound. The coordinates in figures 9 and 10 are x' and y' which are the spatial coordinates x , y rotated by θ . The streamlines around the slat show two regions where the flow separates. First, the region around the bend on the pressure side exhibits what is commonly known as a cove vortex, which shrinks with larger angles of attack. The second region is on the suction side of the slat, which grows with larger angles of attack. The effect of separated flow is a local minimum of c_p shown in figure 11(a).

Table 1: R : radial position of the blade section [m], U_0 : wind speed [m/s], Ω : rotational speed [RPM], θ_p : local pitch angle [$^\circ$], θ_{tw} : local twist angle [$^\circ$], θ : blade angle [$^\circ$], $U_{0,l}$: local inflow velocity, [m/s], δ_0 : boundary layer thickness, mm, and δ_1 : boundary layer displacement thickness, [mm].

R	U_0	Ω	θ_p	θ_{tw}	θ	$U_{0,l}$	δ_0	δ_1
10	4	11.78	1.5	10.77	20.73	12.90	43	33.23
	6	12.30	0	10.77	19.23	14.06	40	33.46
	9	15.32	-1.5	10.77	17.73	18.12	65	43.73
	16	16.23	16.23	10.77	30.83	11.38	133	57.92
36	4	11.78	1.5	1.29	2.79	44.57	40	10.34
	6	12.30	0	1.29	1.29	46.71	45	14.04
	9	15.32	-1.5	1.29	0.21	58.37	55	19.22
	16	16.23	16.23	1.29	12.94	63.01	40	10.34

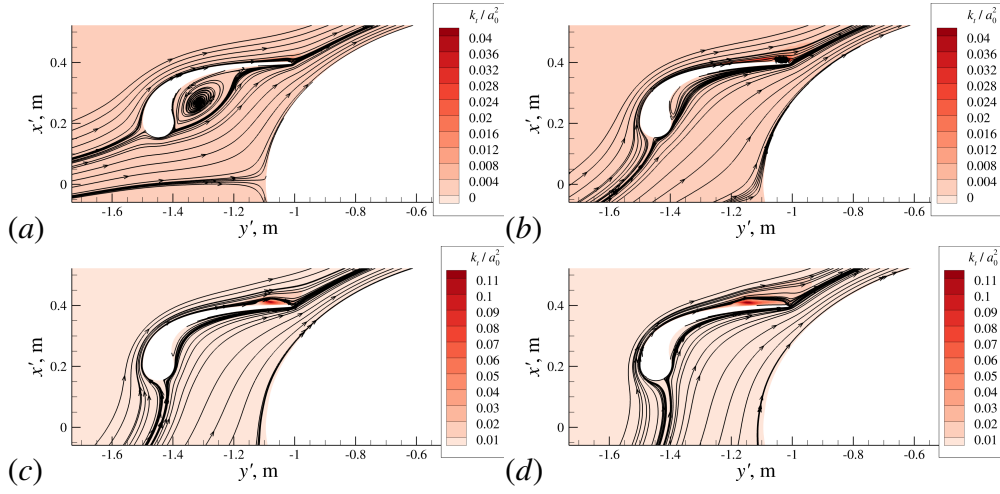


Figure 9: Two-dimensional streamlines of a cross-section of the flow field around the slat at $R = 10$ m. (a) $U_0 = 4$ m/s, (b) $U_0 = 6$ m/s, (c) $U_0 = 9$ m/s, and (d) $U_0 = 16$ m/s.

The streamlines at the outboard blade section show the change of the stagnation point position due to the change of the angle of attack. Most notable is at $U_0 = 16$ m/s, where the pitch angle change results in a decrease of the angle of attack. In contrast, at $U_0 = 16$ m/s, the slat's angle of attack is increased.

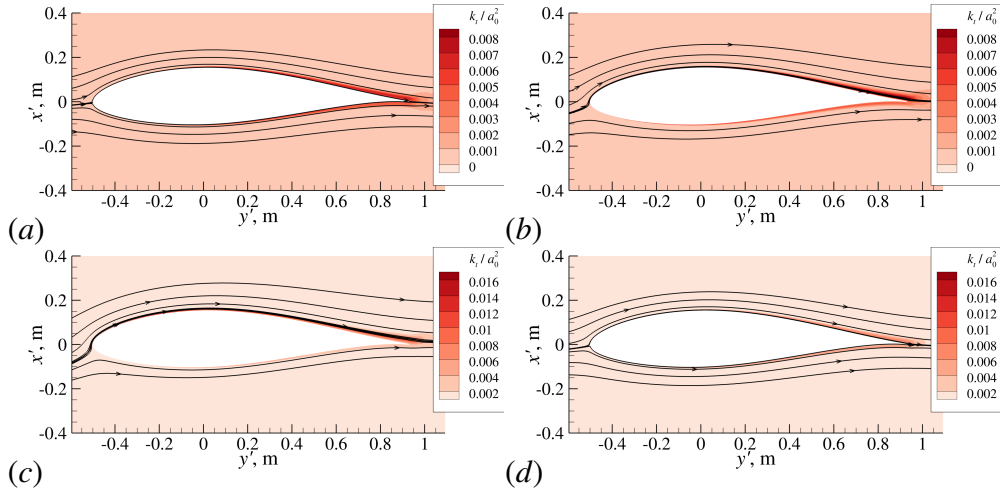


Figure 10: Cross-sectional views of the flow field around the outboard blade section of the Suzlon S88 wind turbine at $R = 36$ m. (a) $U_0 = 4$ m/s, (b) $U_0 = 6$ m/s, (c) $U_0 = 9$ m/s, and (d) $U_0 = 16$ m/s.

For evaluating noise, there are two regions of interest: (1) the slat trailing-

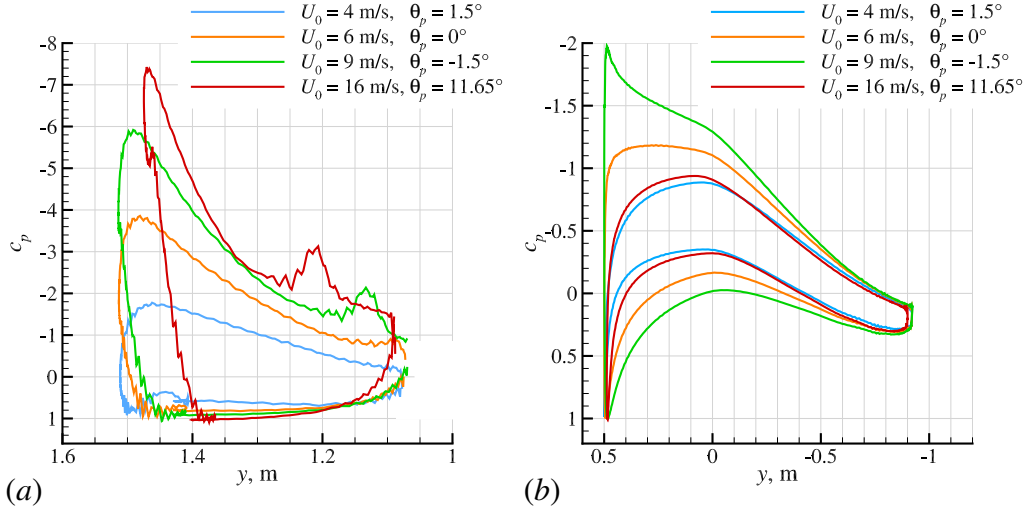


Figure 11: Pressure coefficients of the (a) slat and (b) outboard blade section.

edge that is identified as the possible noise source and (2) the outboard trailing-edge, which is the major contributor to wind turbine noise for an observer on the ground [22]. The size of the FRPM patches of both region is $0.32 \text{ m} \times 0.48 \text{ m} \times 1 \text{ m}$ and the cell size $\Delta x = \Delta y = 0.002 \text{ m}$ and $\Delta z = 0.025 \text{ m}$, which allow for FRPM to resolve a spectrum with a maximum frequency of 1.1 kHz for the slat trailing region and 3.9 kHz for the outboard trailing edge. The patch has a total of 1 552 040 nodes.

4.2 FRPM Turbulence Reconstruction

Figure 12 shows the distribution of enstrophy variance for $U_0 = 6 \text{ m/s}$ as an example. The reconstructed enstrophy is consistently smaller than that of the target. However, their distribution appears to be consistent with each other. The discrepancy is caused by the blade's size, which requires a larger domain size and smaller cell size. A larger domain size or smaller cell size would reconstruct better the wavenumber range of the turbulence field. The spatial lengths for the active trailing-edge are $\ell = (0.002, 0.480) \text{ m}$. Despite the discrepancy in terms of level, the sound pressure level spectra follow the appropriate scaling laws, as will be shown in the next section.

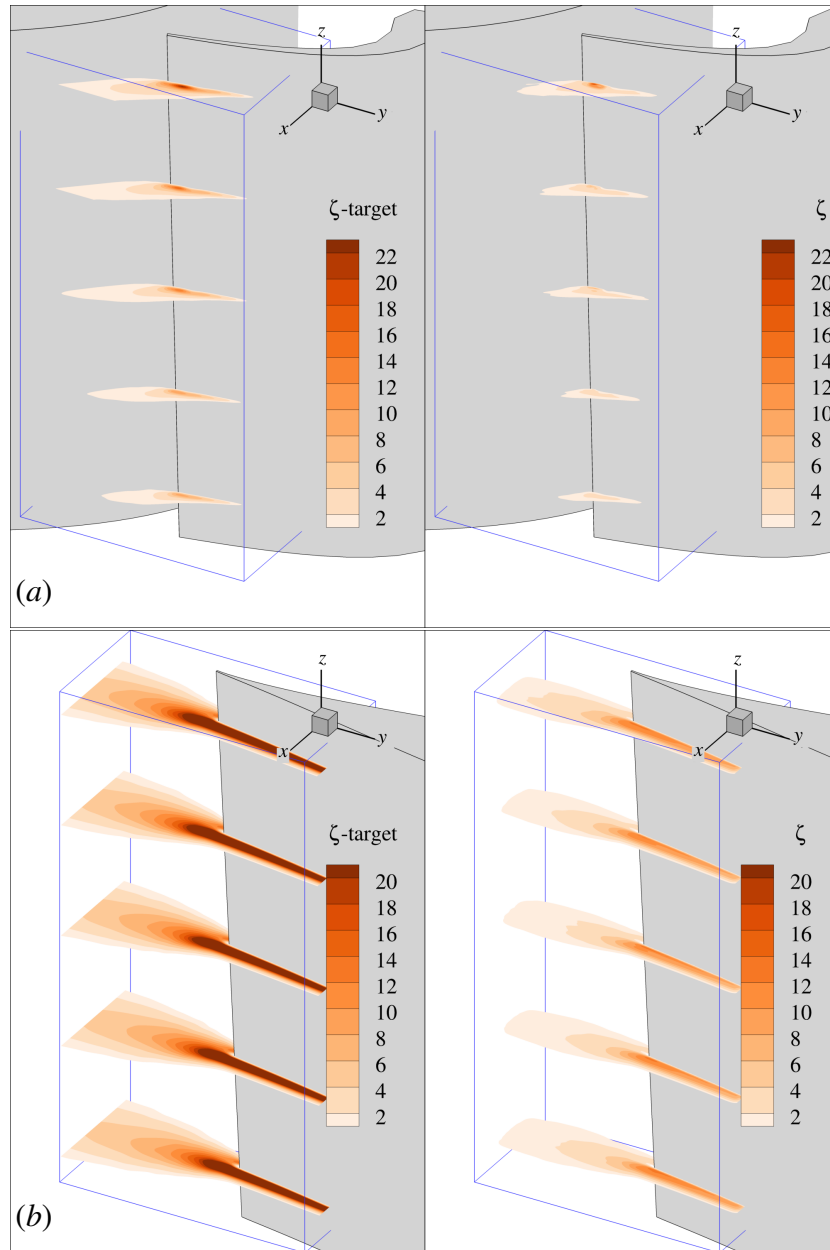


Figure 12: Target and reconstructed enstrophy, ζ for (a) the slat region and (b) outboard trailing-edge.

4.3 FMCAS result

4.3.1 Outboard Trailing-Edge – Trailing-Edge Noise

The overall trailing-edge noise directivities, L_p of the four wind speeds are shown in figure 13. The overall sound pressure levels are the sum of the sound pressure level spectra between $300 \text{ Hz} \leq f_c \leq 4000 \text{ Hz}$. In figure 13(b) the overall directivity is in agreement with the trailing-edge noise scaling of $U_{0,l}^5$ and the directivity angle is corrected with respect to the blade's local pitch angle $\phi - \theta$.

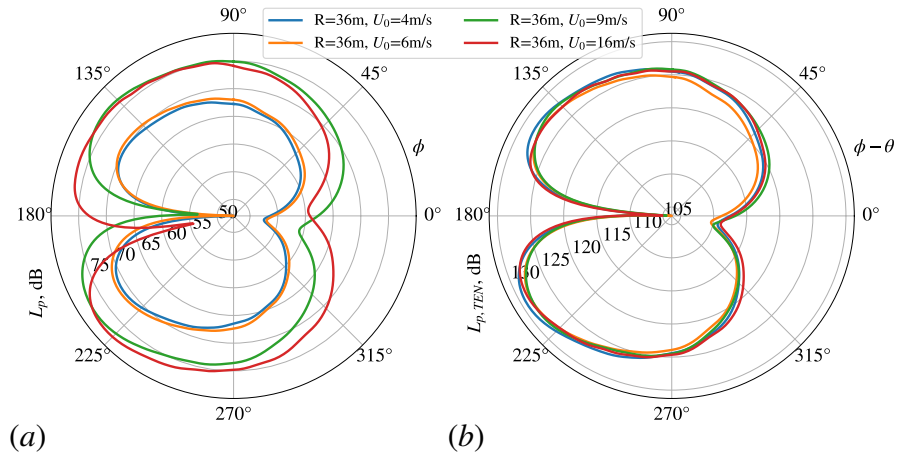


Figure 13: Noise directivity of the outboard trailing-edge (a) unscaled and (b) scaled according to $U_{0,l}^5$.

The sound pressure level spectra in figure 14 is a sample from figure 13 at $\phi - \theta = 208^\circ$, which is the one that contributes to the strongest overall sound pressure level. The scaled trailing-edge noise spectra scales well for $0.3 < f\delta_0/U_{0,l} < 1$. Above the upper range, two spectra with $U_0 = 4 \text{ m/s}$ and 16 m/s collapse well, but not for the others. This discrepancy is caused by the trailing-edge noise scaling characterizing the scales in the inertial range. In contrast, the dissipative range is characterized by the viscous length scale and friction velocity. In short, the trailing-edge noise scaling is expected to cover the low-to-medium frequencies but not the high-frequency range. Figures 13 and 14 show that the trailing-edge noise characteristics can be captured by the present simulation tools.

A comparison of FMCAS result with two-dimensional simulation using DLR's standard CAA code PIANO (Perturbation Investigation of Aerodynamic NOise) is shown in figure 15 for the case of $R = 36 \text{ m}$, $U_0 = 6 \text{ m/s}$. The far-field noise spectrum from PIANO is shown for the directivity angle of $\phi = 275^\circ$, i.e., the ob-

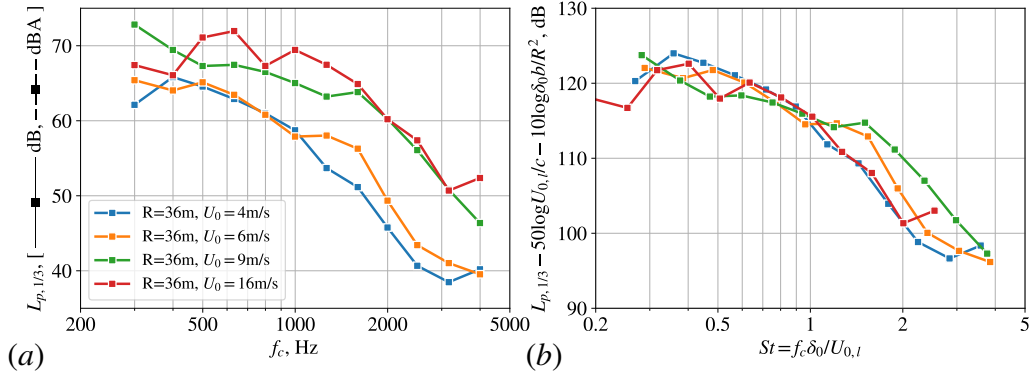


Figure 14: Sound pressure level of the outboard trailing-edge (a) unscaled and (b) scaled according to U_0^5 .

server is at an angle perpendicular to the angle of attack and under the blade section. For a fair comparison, the FMCAS far-field noise spectrum at the same angle is shown in figure 15 along with $\phi - \theta = 208^\circ$, or $\phi = 208^\circ$. The PIANO spectrum plateaus at approximately 55 dB for $f \geq 1$ kHz, whereas the FMCAS result decays further. FMCAS failed to reach the frequency where the spectrum reached its peak. However, with A-rating, the spectral peak will be at a higher frequency because the A-rating decreases the spectral level by 11 dB at 200 Hz. In general, FMCAS and PIANO spectra follow the same trend for $300 \text{ Hz} < f_c < 1000 \text{ Hz}$ at $\phi = 275^\circ$. The FMCAS spectrum at $\phi = 208^\circ$ decays in the same way as the spectrum at $\phi = 275^\circ$ and is 5 dB larger due to the directivity. The advantage of

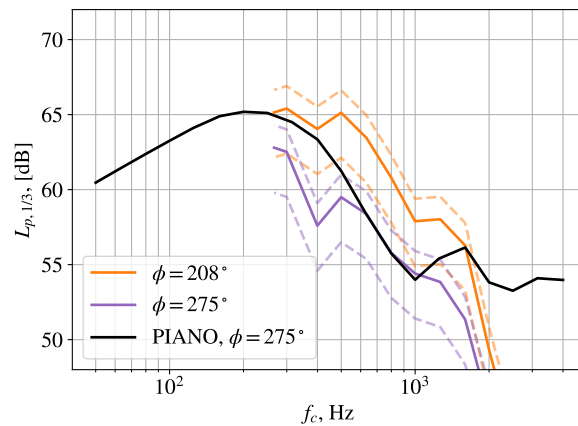


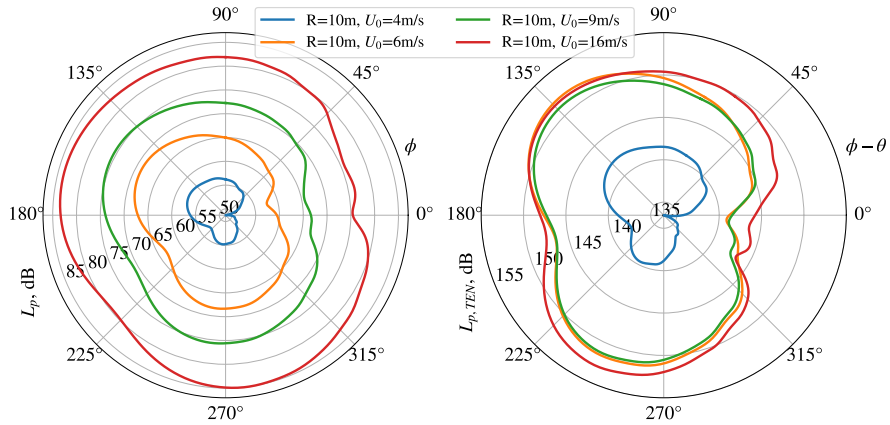
Figure 15: Comparison of sound pressure level calculated using PIANO and FRPM/FMCAS

using FRPM/FMCAS is that, unlike PIANO, the governing equations are resolved only on the boundaries. Hence, a three-dimensional domain can be resolved with fewer computer resources. In total, the FRPM calculation took 4 hours and 48 minutes on an Intel XEON W-2135 3.75 GHz using a single thread, and FMCAS were calculated for each frequency in parallel, taking 5 hours and 31 minutes on a 32 cores AMD EPYC 7601 2.2 GHz.

4.3.2 Slat Trailing-Edge – Slat Noise

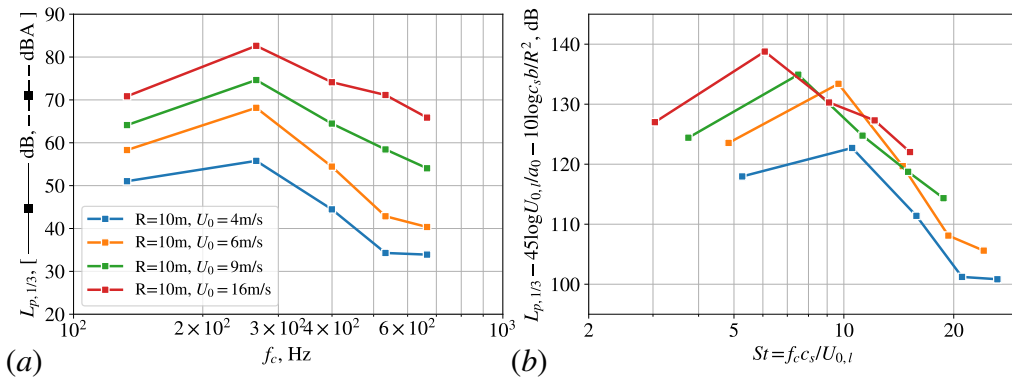
The unscaled and $U_{0,l}^5$ scaled directivity of the slat noise is shown in figure 16. This directivity is an integral result with limits $100 \text{ Hz} < f < 600 \text{ Hz}$. The scaled directivity, $L_{p,TEN} = L_p - 50\log(U_{0,l}/a_0) - 10\log(c_s b/R^2)$, fits for all cases except $R = 10 \text{ m}$, $U_0 = 4 \text{ m/s}$. The reason for this exception is not fully clear. The shape of the directivity of $R = 10 \text{ m}$, $U_0 = 4 \text{ m/s}$ is similar to the other cases, and only the magnitudes do not follow the scaling argument. The flow field of cases $R = 10 \text{ m}$, $U_0 > 4 \text{ m/s}$ feature a significantly reduced cove vortex but increased separation bubble close to the trailing-edge on the suction side, whereas at $R = 10 \text{ m}$, $U_0 = 4 \text{ m/s}$ the cove vortex is more pronounced, c.f. figure 9. These flow characteristics might explain the inconsistency of the applied velocity scaling. Regardless, the maxima of the upper and lower directivity lobes are located at $\phi - \theta = 135^\circ$ and 245° , respectively, and the maximum levels between the upper and lower lobes have no clear distinction.

The sound pressure level spectra are extracted from $\phi - \theta = 135^\circ$ and shown in figure 17 for both unscaled and scaled. The sound pressure level at the negative slope scales with $U_{0,l}^{4.5}$ instead of the fifth power. This scaling follows the typical slat noise scaling [23] and is different from the scaling applied to the overall noise directivity. The difference can be due to the simulation's low spectral resolution, which has a frequency width of $\Delta f \approx 133 \text{ Hz}$ and the narrow spectral range not containing enough energy to capture the same scaling. Nevertheless, the position of the maxima of the directivity lobes is unaffected by the scaling method. It is dependent only on the geometry, as shown by the directivity pattern collapsing together with the directional angles $\phi - \theta$. Overall, it can be concluded that the present simulation tools can well capture the slat noise characteristics.



(a) (b)

Figure 16: Slat noise directivity (a) unscaled and (b) scaled to U_0^5 .



(a) (b)

Figure 17: Slat noise directivity (a) unscaled and (b) scaled to $U_{0,l}^{4.5}$.

5 Discussion

Wind turbine noise is predicted based on the spectral results described in section 4 using a new, simple and fast, prediction method described in Refs. [24, 25, 26]. The prediction method treats each blade in the same condition, and each blade is divided into a finite span blade element. The sound spectra at various conditions due to the blade's revolution are emulated from the input spectra. The acoustic impact on the ground is a superposition of the sound source from each blade element. In the present study, only two segments are available. Hence, the final acoustic level is not representative of a rotor blade at full length. This exercise aims to rank the level of slat noise and outboard trailing-edge noise at an arbitrary ground position.

The A-rated overall sound pressure level as experienced by an observer on the ground at a position x_o, y_o is mapped in figures 18-21 for wind speeds of $U_0 = 4$ m/s to 16 m/s, respectively. The sound maps in these figures are the average over a single rotation of the rotor blades. In (a) the sound map is explicitly the result of the slat noise, and in (b) it is the result of the outboard trailing-edge noise. In (c) the sound map is the result of the superposition of both noise sources. The red vertical line represents the rotor. The wind is moving from the left to the right of the figures. The dashed circle represents observers at a distance equal to the sum of the wind turbine height and the wind turbine rotor radius, i.e., 124 m, of which the downwind position is defined in IEC 64100-11 as the standard observer.

At the standardized observer location, the contribution of the slat noise and the outboard trailing-edge noise is shown by the A-rated overall sound pressure level (L_p , dBA) in figure 22. With increasing wind speeds, the slat noise level increases more rapidly than the outboard trailing-edge noise, such that the slat noise is louder than the outboard trailing-edge noise for $U_0 = 16$ m/s. Note that slat noise contributions are negligible only for the lowest wind speed $U_0 = 4$ m/s. In contrast, the overall sound pressure levels are increasingly affected by the slat's presence at the higher wind speeds.

Figure 23 shows the overall sound pressure level of each U_0 to Θ , the angle the ground observer is facing the wind turbine. In this figure, $\Theta = 0^\circ$ indicates the downwind position, and Θ increases in the counter-clockwise direction of the circle in figure 18. The observer remains at the standard distance of 124 m from the wind turbine.

At $U_0 = 4$ m/s, the low slat noise level gives approximately 17 dB less than the outboard trailing-edge noise. At $U_0 = 6$ m/s and $U_0 = 9$ m/s the slat contributes to an additional 0.5-1 dBA and 1-2 dBA, respectively. The slat noise is maximum upwind of the wind turbine, however the outboard trailing-edge remains to be the predominant sound source with its maximum radiation downwind of the wind turbine. One can also observe two local noise peaks at $\Theta = 90^\circ$ and 270° , or along

the rotor plane.

For $6 \text{ m/s} \leq U_0 \leq 9 \text{ m/s}$, the maximum radiation of the slat noise is upwind of the wind turbine, whereas the outboard trailing-edge noise is maximum directly downwind of the wind turbine. the combined sound sources are predominated by the outboard trailing-edge noise.

The slat noise contribution to the total is negligible for $U_0 = 4 \text{ m/s}$. For $U_0 = 6 \text{ m/s}$ and $U_0 = 9 \text{ m/s}$, the slat contributes to an additional 0.5-1 dBA and 1-2 dBA, respectively.

At $U_0 = 16 \text{ m/s}$, the slat noise is louder than the trailing-edge noise at all Θ . Furthermore, the combined source's maximum noise level is upwind of the wind turbine, similar to the slat noise. The difference of overall sound pressure levels at the upwind and downwind at $U_0 = 16 \text{ m/s}$ is approximately 1.5 dBA. However, this wind speed can be considered as an *off-design* condition, because the blade is in the fully loaded region for $U_0 > 11 \text{ m/s}$ and on-site this wind speed is rarely achieved.

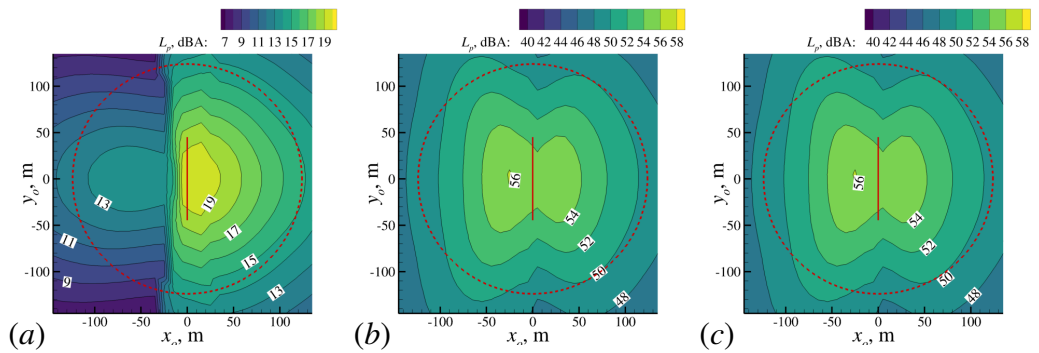


Figure 18: With $U_0 = 4 \text{ m/s}$, the sound footprint from (a) slat, (b) outboard trailing-edge, and (c) combination of both.

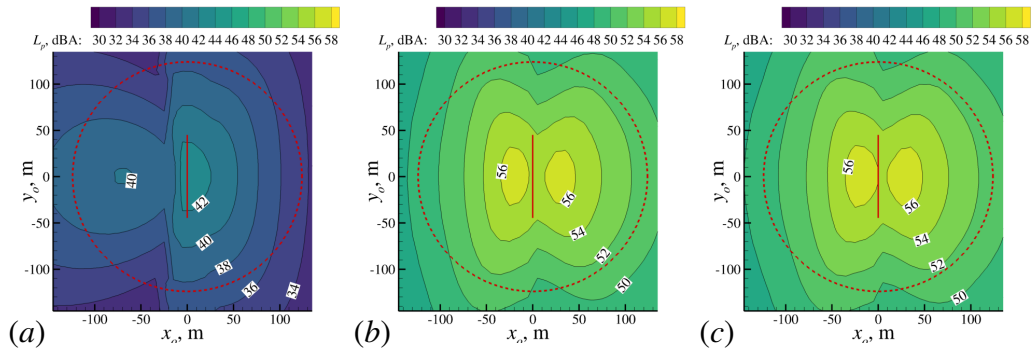


Figure 19: With $U_0 = 6$ m/s, the sound footprint from (a) slat, (b) outboard trailing-edge, and (c) combination of both.

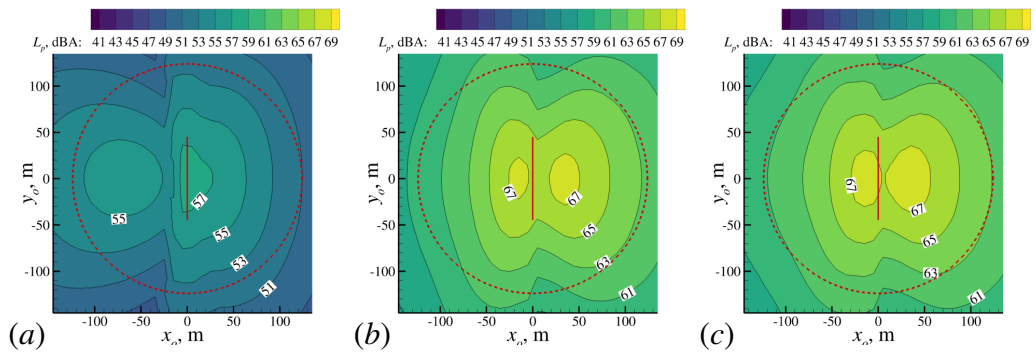


Figure 20: With $U_0 = 9$ m/s, the sound footprint from (a) slat, (b) outboard trailing-edge, and (c) combination of both.

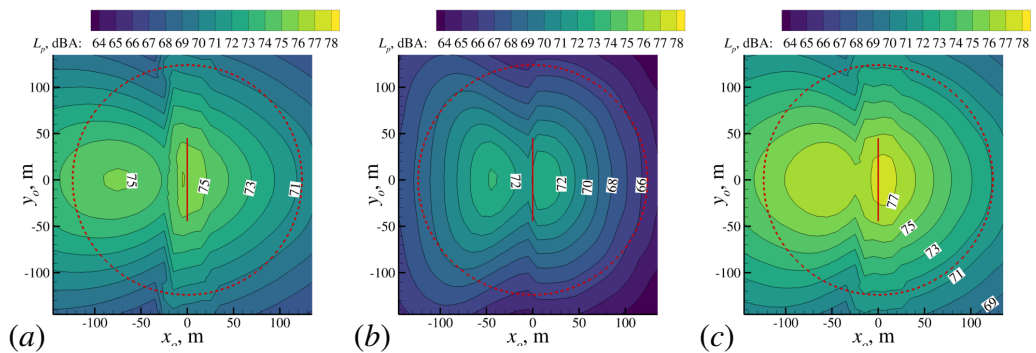


Figure 21: With $U_0 = 16$ m/s, the sound footprint from (a) slat, (b) outboard trailing-edge, and (c) combination of both.

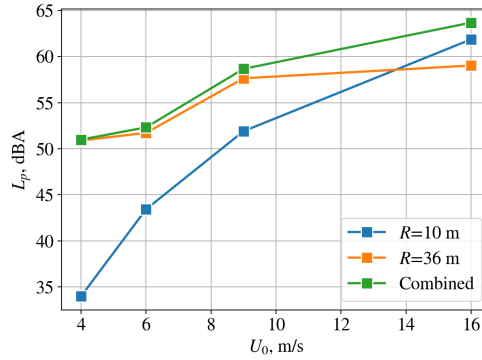


Figure 22: A-rated overall sound pressure level vs wind speed, U_0 .

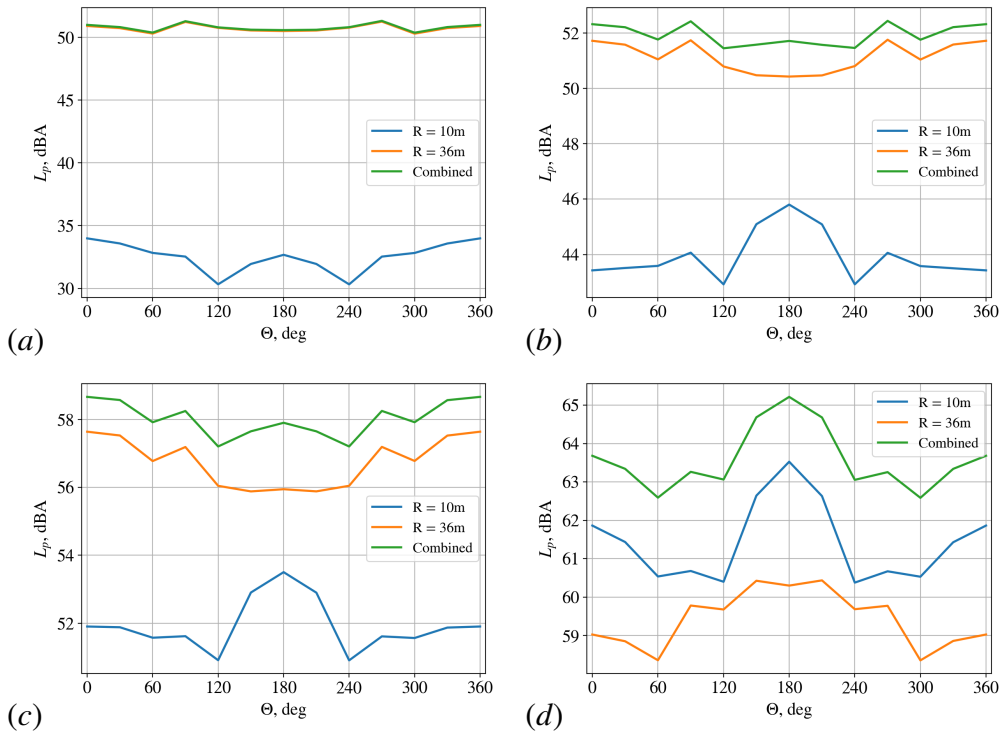


Figure 23: A-rated overall sound pressure levels with respect to the azimuth angle, Θ ; (a) $U_0 = 4$ m/s, (b) $U_0 = 6$ m/s, (c) $U_0 = 9$ m/s, and (d) $U_0 = 16$ m/s.

6 Conclusions

The FRPM/FMCAS prediction method was successfully validated with the experiments conducted in the AWB. Numerical simulations of a volume encompassing much of the trailing-edge and the flap-side edge show good agreement with the measured sound pressure level. An analysis with a narrow region to focus on the flap side-edge noise show good agreement for the case with negative flap deflection, less agreeable for the positive flap deflection. The disagreement is due to the measured spectra affected by the thicker boundary layer and adverse pressure gradient.

Sections of a Suzlon S88 rotor blade, with blade length $R = 44.45$ m, were evaluated to rank the slat noise trailing-edge and the outboard trailing-edge using DLR's FRPM/FMCAS noise prediction tool. The findings are summarized below

1. FRPM/FMCAS simulation captured the trailing-edge noise and slat noise characteristics as determined from their respective scaling relations.
2. There is good agreement between FMCAS results and two-dimensional PIANO results.
3. The maximum radiation of the outboard trailing-edge noise has a directivity angle on the lower lobe at a directivity angle of $208^\circ +$ the blade's pitch angle.
4. The radiation maxima of the slat noise exist at the upper and lower lobes. The upper lobe maximum is at the directivity angle of $135^\circ +$ the blade's pitch angle and the lower lobe maximum is at the directivity angle of $245^\circ +$ the blade's pitch angle.
5. By comparing the A-rated overall sound pressure levels, the sound emanating from 1 m span sections of the outboard rotor represented by the profile at $R = 36$ m is stronger than that emanating from the slat trailing-edge represented by $R = 10$ m with the same span length for $-1.5^\circ \leq \theta_p \leq 1.5^\circ$.
6. The slat noise at higher wind speed of $U_0 = 16$ m/s is larger for all directivity angles ϕ , except for a narrow range of $204^\circ < \phi < 246^\circ$.

The acoustic of the rigid inboard slat and the outboard trailing-edge at various ground positions 124 m away from the wind turbine's hub was evaluated using a fast and simple, non-empirical method. The method uses the noise calculation of a static model by FRPM/FMCAS to emulate the wind turbine blade's rotating conditions. The slat noise contribution to the combined noise source is negligible at $U_0 = 4$ m/s. The slat noise adds 1 dBA to the outboard trailing-edge noise at

$U_0 = 9$ m/s. Slat noise levels at $U_0 = 16$ m/s are higher compared to the outboard trailing-edge noise, however this wind speed is off-design, because the blades are fully loaded at $U_0 > 11$ m/s.

The advantage of FRPM/FMCAS is that the Helmholtz equation is resolved along the far-field boundary. Hence, scaling up the problem does not require as much resource as resolving a volumetric domain. Furthermore, using the emulation method, the wind turbine noise at an arbitrary position can be calculated quickly. Although not performed here, a full-scale analysis of a blade is possible. As such, the tools presented in this work can be used to design low-noise wind turbines efficiently.

Acknowledgement

The authors' are grateful for the support from Forwind Hannover for the flap side-edge CFD simulations and wind tunnel measurements. This study, part of the project SmartBlades 2.0, was funded by the German Ministry for Economic Affairs and Energy (BMWi). Funding reference no. 0324032D.

References

- [1] B. Ll. Jones, W. H. Lio, and J. A. Rossiter. Overcoming fundamental limitations of wind turbine individual blade pitch control with inflow sensors: Overcoming fundamental limitations of wind turbine individual blade pitch control with inflow sensors. *Wind Energy*, 21(10):922–936, October 2018.
- [2] Alexandre Suryadi, Christoph Jätz, Michaela Herr, and Jörg Seume. Identifying the flap side-edge noise contribution of a wind turbine blade section with an active trailing-edge. In *International Conferences of Wind Turbine Noise 2021*, May 2021.
- [3] Roland Ewert. Broadband slat noise prediction based on CAA and stochastic sound sources from a fast random particle-mesh (RPM) method. *Computers & Fluids*, 37(4):369–387, May 2008.
- [4] R. Ewert, J. Dierke, J. Siebert, A. Neifeld, C. Appel, M. Siefert, and O. Kornow. CAA broadband noise prediction for aeroacoustic design. *Journal of Sound and Vibration*, 330(17):4139–4160, August 2011.
- [5] Nils Reiche, Roland Ewert, and Jan Delfs. Realization of Arbitrary Vorticity Spectra using Generic Stochastic Turbulence. In *22nd AIAA/CEAS Aeroacoustics Conference*, Lyon, France, May 2016. American Institute of Aeronautics and Astronautics.
- [6] Nils Reiche, Roland Ewert, Markus Lummer, and Jan Delfs. Fast Multipole Boundary Element Method with Stochastic Sources for Broadband Noise Simulation. In *23rd AIAA/CEAS Aeroacoustics Conference*, Denver, Colorado, June 2017. American Institute of Aeronautics and Astronautics.
- [7] Markus Lummer, Rinie A. Akkermans, Christoph Richter, Carsten Präber, and Jan Delfs. Validation of a Model for Open Rotor Noise Predictions and Calculation of Shielding Effects using a Fast BEM. In *19th AIAA/CEAS Aeroacoustics Conference*, Berlin, Germany, May 2013. American Institute of Aeronautics and Astronautics.

- [8] Nils Reiche, Markus Lummer, Roland Ewert, and Jan W Delfs. Synthetic Turbulence imposed as Boundary Condition for Fast Multipole BEM. In *Waves 2019*, Vienna, Austria.
- [9] Christof Rautmann. Generic Airfoil Trailing-Edge Noise Prediction using Stochastic Sound Sources from Synthetic Turbulence. In *20th AIAA/CEAS Aeroacoustics Conference*, page 21, Atlanta, Georgia, 2014. AIAA.
- [10] A. Wohlbrandt, N. Hu, S. Guérin, and R. Ewert. Analytical reconstruction of isotropic turbulence spectra based on the Gaussian transform. *Computers & Fluids*, 132:46–50, June 2016.
- [11] Nils Reiche, Markus Lummer, Roland Ewert, and Jan W Delfs. Anisotropic synthetic turbulence and Fast Multipole BEM for high-lift noise prediction. *numerical methods*, page 19.
- [12] Michaela Herr, Karl-Stephane Rossignol, Jan Delfs, Nicolas Lippitz, and Michael Mößner. Specification of Porous Materials for Low-Noise Trailing-Edge Applications. In *20th AIAA/CEAS Aeroacoustics Conference*, Atlanta, GA, June 2014. American Institute of Aeronautics and Astronautics.
- [13] Syamir A. Showkat Ali, Máté Szoke, Mahdi Azarpeyvand, and Carlos R. Ilario da Silva. Turbulent Flow Interaction with Porous Surfaces. In *2018 AIAA/CEAS Aeroacoustics Conference*, Atlanta, Georgia, June 2018. American Institute of Aeronautics and Astronautics.
- [14] Karl-Stéphane Rossignol, Alexandre Suryadi, Michaela Herr, Johannes Schmidt, and Jörn Tychsen. Experimental Investigation of Porous Materials for Trailing-Edge Noise Reduction. *International Journal of Aeroacoustics*, 19(6-8):365–384, 2020.
- [15] M. Herr. Experimental Study on Noise Reduction through Trailing Edge Brushes. In Ernst Heinrich Hirschel, W. Schröder, Kozo Fujii, Werner Haase, Bram Leer, Michael A. Leschziner, Maurizio Pandolfi, Jacques Periaux, Arthur Rizzi, Bernard Roux, Hans-Josef Rath, Carsten Holze, Hans-Joachim Heinemann, Rolf Henke, and Heinz Hönlinger, editors, *New Results in Numerical and Experimental Fluid Mechanics V*, volume 92, pages 365–372. Springer Berlin Heidelberg, Berlin, Heidelberg, 2006.
- [16] Alexandre Suryadi, Susanne Martens, and Michaela Herr. Trailing Edge Noise Reduction Technologies for Applications in Wind Energy. In *23rd AIAA/CEAS Aeroacoustics Conference*, Denver, Colorado, June 2017. American Institute of Aeronautics and Astronautics.

- [17] Pieter Sijtsma. CLEAN Based on Spatial Source Coherence. *International Journal of Aeroacoustics*, 6(4):357–374, December 2007.
- [18] Thomas F Brooks and William M. Humphreys Jr. Flap-edge aeroacoustic measurements and predictions. *Journal of Sound and Vibration*, page 44, 2003.
- [19] Nan Hu and Michaela Herr. Characteristics of wall pressure Fluctuations for a Flat plate turbulent boundary layer with pressure gradients. In *22nd AIAA/CEAS Aeroacoustics Conference*, page 2749, Lyon, France, May 2016. AIAA.
- [20] Ana Manso Jaume and Jochen Wild. Aerodynamic Design and Optimization of a High-Lift Device for a Wind Turbine Airfoil. In Andreas Dillmann, Gerd Heller, Ewald Krämer, Claus Wagner, and Christian Breitsamter, editors, *New Results in Numerical and Experimental Fluid Mechanics X*, volume 132, pages 859–869. Springer International Publishing, Cham, 2016.
- [21] D. Schwamborn, T. Gerhold, and R. Kessler. DLR-TAU code - an overview. In *1st ONERA/DLR Aerospace Symposium, Paris, 21.-24. Juni 1999*, pages S4–2–S4–10, 1999.
- [22] Stefan Oerlemans, Murray Fisher, Thierry Maeder, and Klaus Kögler. Reduction of Wind Turbine Noise Using Optimized Airfoils and Trailing-Edge Serrations. *AIAA Journal*, 47(6):1470–1481, June 2009.
- [23] W. Dobrzynski and M. Pott-Pollenske. Slat noise source studies for farfield noise prediction. In *7th AIAA/CEAS Aeroacoustics Conference and Exhibit*, Maastricht, Netherlands, May 2001. American Institute of Aeronautics and Astronautics.
- [24] Benjamin W. Fassmann, Nils Reiche, Roland Ewert, Michaela Herr, and Jan Delfs. Evaluation of Wind Turbine Noise based on Numerical Simulation Methods. In *2018 AIAA/CEAS Aeroacoustics Conference*, Atlanta, Georgia, June 2018. American Institute of Aeronautics and Astronautics.
- [25] Benjamin Faßmann, Michaela Herr, Roland Ewert, and Jan Delfs. Emulation of Sound Pressure Level Spectra Based on Numerical Data. In Andreas Dillmann, Gerd Heller, Ewald Krämer, Claus Wagner, Cameron Tropea, and Suad Jakirlić, editors, *New Results in Numerical and Experimental Fluid Mechanics XII*, volume 142, pages 739–748. Springer International Publishing, Cham, 2020.

- [26] Christina Appel, Benjamin Fassmann, Shy-Yea Lin, and Michaela Herr. CAA-basierte Schallvorhersage für Windkraftanlagen. In *Fortschritte der Akustik - DAGA 2020*, Tagungsband DAGA, page 4, Hannover, 2020. Deutsche Gesellschaft für Akustik e.V.

A Third-octave Sound Pressure Level

The sound pressure level, L_p , is a measure of the mean square level of pressure fluctuations relative to a reference pressure and is defined as

$$L_p, \text{dB} = 20 \log_{10} \left(\frac{p'_{rms}}{20 \mu\text{Pa}} \right), \quad (23)$$

where $p'^2_{rms} = \int_{-\infty}^{\infty} \Phi_{pp}(f) df$ is the integration of the power spectral density of the pressure fluctuations with respect to the frequency.

The one-third octave frequency band is defined by convention around center frequencies $f_c = 2^{n/3} 1000$ Hz, where n is an integer value. The mean square level of pressure fluctuations p'^2_{rms} , around f_c is defined as

$$p'^2_{rms}(f_c) = \int_{f_l}^{f_u} \Phi_{pp}(f) df \quad (24)$$

with $f_u = 2^{1/6} f_c$ and $f_l = 2^{-1/6} f_c$.

The result of the FMCAS simulation is a narrow frequency band spectrum $dp'^2_{rms} = \Phi_{pp}(f) df$ that has to be translated to the one-third octave spectrum to follow the convention in engineering acoustics. Introducing f/f into the integrand on the right-hand side of Eqn. 24 leads to

$$p'^2_{rms}(f_c) = \int_{f_l}^{f_u} \Phi_{pp}(f) f d \ln f, \quad (25)$$

differentiating once on both sides gives

$$dp'^2_{rms}(f_c) = \Phi_{pp}(f) f d \ln f, \quad (26)$$

which is the narrow-band sound pressure level at $f = f_c$. Substituting the integration limits to the differential variable $d \ln f$ leads to

$$\begin{aligned} d \ln f &= \ln f_u - \ln f_l \\ &= \frac{1}{3} \ln 2 \end{aligned} \quad (27)$$

with $\ln f_u = 1/6 \ln 2 + \ln f_c$ and $\ln f_l = -1/6 \ln 2 + \ln f_c$. Equation 27 shows that the integration limits are independent of f . As a bound variable, f on the right-hand side of Eq. 26 can be substituted by f_c , so that the one-third octave band mean square pressure level can be expressed as

$$dp_{rms}^{\prime 2} = \Phi_{pp}(f_c) f_c \frac{\ln 2}{3}. \quad (28)$$

The first two factors on the right-hand side can be expressed as $\Phi_{pp}(f_c) f_c = \Phi_{pp}(f_c) \partial f i$, where i is an integer multiplier and ∂f is a finite narrow band frequency width. This expression relates the one-third octave band mean square pressure fluctuations to that of the narrow band. The advantage of expressing Eqn. 28 is that the FMCAS simulation does not need to resolve all frequencies in the narrowband spectrum. The FMCAS calculations can be limited to the frequencies that best approximate the one-third octave band center frequencies.

The overall sound pressure level is a measure of

$$p_{rms}^{\prime 2}(\phi) = \int_{-\infty}^{\infty} \Phi_{pp}(f, \phi) df \quad (29)$$

Using Eqn. 28, the overall sound pressure level can be expressed as

$$p_{rms}^{\prime 2}(\phi) = \sum_i^N dp_{rms}^{\prime 2}(\phi, f_{c,i}) = \sum_i^N \Phi_{pp}(\phi, f_{c,i}) f_{c,i} \frac{\ln 2}{3}, \quad (30)$$

where $f_{c,i}$ denotes the i^{th} one-third active center frequency. Given $0^\circ < \phi \leq 360^\circ$, $p_{rms}^{\prime 2}(\phi)$ gives us the non-normalized directivity of the overall sound pressure level. The angle ϕ originates from the trailing-edge, and it increases such that the upper arc $0^\circ < \phi < 180^\circ$ covers the airfoil's suction side and the lower arc covers the pressure side.